

TURN A HIGHLY-REFLECTIVE METAL INTO AN OMNIDIRECTIONAL BROADBAND ABSORBER BY COATING A PURELY-DIELECTRIC THIN LAYER OF GRATING

Feng Zhang^{1, †}, Liu Yang^{1, 2, †}, Yi Jin¹, and Sailing He^{1, 2, *}

¹Centre for Optical and Electromagnetic Research, JORCEP, Zhejiang Provincial Key Laboratory for Sensing Technologies, Zhejiang University, Hangzhou 310058, China

²ZJU-SCNU Joint Research Center of Photonics, South China Normal University, Guangzhou 510006, China

Abstract—We show that a metal can be turned into a broadband and omnidirectional absorber by coating a purely-dielectric thin layer of grating. An optimal design for such an absorber is proposed by putting a dielectric slot waveguide grating (SWG) on the metallic substrate. The SWG consists of two germanium nanowires (Ge NWs) separated by a sub-100 nm slot in each period. Average absorption reaches 90% when the incident angle varies between 0° and 80° over a broad wavelength range from 300 nm to 1400 nm. Multiple optical mechanisms/effects, namely, diffraction, waveguiding in the high-index Ge NWs and low-index air slot, Fabry-Perot resonances as well as surface plasmon polaritons (SPPs), are identified to govern the absorption characteristics of the present absorber. The designed absorber with such a dielectric grating is easier to fabricate as compared with other absorbers with metallic nanostructures, and has potential applications in, e.g., solar cells and photodetectors.

1. INTRODUCTION

Perfect absorption of light without any reflection or transmission is of critical importance for optical energy conversion, especially in visible and near-infrared regime covering the main solar spectrum. In order to efficiently convert solar energy into electrical (or thermal)

Received 28 October 2012, Accepted 15 November 2012, Scheduled 21 November 2012

* Corresponding author: Sailing He (sailing@ieee.org).

† Feng Zhang and Liu Yang contributed equally to this work.

energy, which people can use directly, broadband perfect absorbers are required to harvest and absorb as many photons as possible [1–3]. Recent advances in micro-/nano-technology become helpful to achieve many flexible designs of broadband perfect absorbers based on micro-/nano-structures [2, 4]. Metallic nanostructures supporting surface plasmon polaritons (SPPs) are most widely employed due to their strong ability to harvest and localize photons in a subwavelength region [2, 5, 6], where the resonant photons can be strongly absorbed by the compositional metallic and/or lossy dielectric material. Recently, another interesting absorber, based on metallic metamaterials, has been suggested [7]. Unlike plasmonic absorbers, both electric and magnetic resonances can be excited simultaneously in the metamaterial absorbers and complete absorption can be achieved [4, 8, 9]. However, the bandwidth is usually very narrow, due to the resonant characteristics [10–16]. By simply mixing together different resonators with different resonant frequencies, broad absorption spectrum can be achieved [17–22]. Very recently, Søndergaard et al. proposed a non-resonant broadband absorber based on ultra-sharp convex grooves via adiabatic nanofocusing of gap SPPs [23]. Another non-resonant absorbers proposed by Cui et al. was made of a sawtoothed anisotropic metamaterial via slowlight modes and a large bandwidth of about 86% of its central wavelength was achieved [24] (experimental verification in the microwave regime can be found in Ref. [25]). Low-bandgap semiconductors themselves are also good broadband absorbers, e.g., Si, Ge, and will have much better antireflection and absorption properties if micro-/nano-structures are formed, e.g., microwires [26], nanowires/holes [27–29], nanotips [30], nanocones [31], etc. A hybrid dielectric-metal core-shell grating structure over a metallic substrate was used in Ref. [32] to achieve broadband, omnidirectional, and polarization-independent absorption by combining two kinds of optical modes, namely, Bloch and SPP modes.

In the present paper we report a novel absorption structure by simply putting a purely-dielectric thin layer of grating on a metallic substrate. We will also show that by combining multiple physical effects together, an enhanced absorption and ultrabroad bandwidth can be achieved. Our optimal structure consists of a gold (Au) substrate covered with a dielectric Slot Waveguide Grating (SWG, dielectric grooves are much easier to fabricate than metallic grooves [23]), which contains two Ge nanowires (NWs) with a small separation between them in each period. Compared with a grating structure with only one NW in each period, our SWG-based structure has a flatter total absorption spectrum over a broad wavelength range from 300 to 1400 nm and is also angle-insensitive (from 0 to 80°).

2. STRUCTURE AND THEORETICAL MODEL

Our proposed SWG based absorber is shown schematically in Figure 1(a), where there are two Ge NWs separated by d in each period on a gold (Au) substrate. Compared with silicon (Si) often used in the solar cell industry, Ge is more expensive. However, Ge has a much higher absorption coefficient over a much broader wavelength range than Si. On the other hand, Ge is also a solar material often used in multi-junction thin-film solar cells to absorb photons in the near-infrared wavelength range [33]. Thus we choose Ge instead of Si as the main absorbing material. In the nanostructure shown in Figure 1(a), the Ge NW widths are set equal, i.e., $w_1 = w_2$, unless otherwise specified. The grating height is set to h . As a reflector, the Au substrate is assumed to be thick enough to prevent any transmission through it. Due to the rather small separation between the two NWs in each period, slot waveguide modes together with some interesting optical responses can be generated in our structure. In order to focus on the analysis on these effects, we fix the grating period to 620 nm, i.e., $P = 620$ nm, throughout the paper. For comparison, a grating with only one NW of width, w , in each period is plotted in Figure 1(b) with the same period, $P = 620$ nm, and NW height, h .

We employed the finite element method (FEM) [34] to simulate the optical responses when a plane wave is incident from the top with an incident angle, θ , and a wave vector, k_0 , as shown in Figure 1. The light wavelength, λ , is chosen from 300 to 1500 nm, beyond which Ge has little absorption. Here, only transverse-magnetic (TM) polarization is considered with magnetic field, H , perpendicular to the x - z plane

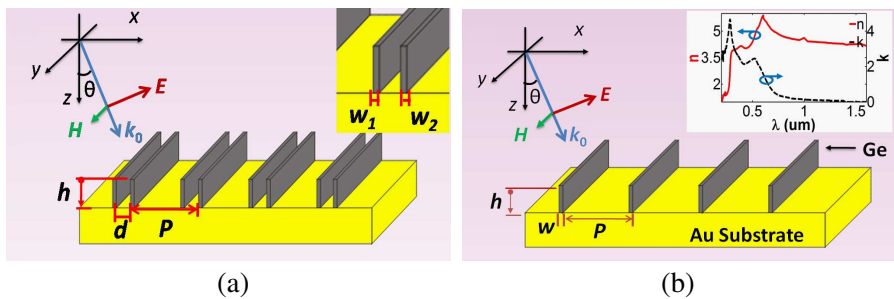


Figure 1. Schematic diagram of (a) an SWG-based absorber with two NWs in each period; (b) an absorber with only one NW in each period. A TM-polarized plane wave is incident from the top with an incident angle, θ , and a wave vector, k_0 . The inset of Figure 1(b) shows dielectric constant ($n - i \cdot k$) of Ge [35].

in order to excite the polarization-sensitive slot waveguide and SPP modes, and investigate their effects on the optical performances. In the simulation, the dielectric constant of Ge and Au are both chosen from previously published experimental data [35]. The former is shown in the inset of Figure 1(b). Through numerical simulation, we can easily get the electric field distribution, E , as well as the partial absorptions in each of the compositional material, A_{Ge} and A_{Au} from the following equation:

$$A_{\text{Ge or Au}} = \frac{\iint_{\text{Ge or Au}} \frac{\pi c}{\lambda} \cdot \text{Im}(\varepsilon_{\text{Ge or Au}}) |E|^2 dx dz}{\text{Source power}} \quad (1)$$

where $\text{Im}(\varepsilon)$ is the imaginary part of the material's dielectric constant. Since there is no other absorbing materials in our structure, the total absorption can be calculated by $A = A_{\text{Ge}} + A_{\text{Au}}$. In comparison, $A = 1 - R$ is not a good way to calculate the total absorption. Since there are many optical mechanisms/effects to be excited within this structure, including diffraction (Rayleigh anomalies), waveguiding in the high-index Ge NWs and low-index air slot, Fabry-Perot (FP) resonances and SPPs, if the reflection is monitored far from the top Ge NWs, some near-field optical behaviors cannot be detected with $A = 1 - R$ and the result may become quite different from that calculated by $A = A_{\text{Ge}} + A_{\text{Au}}$, unless the reflection monitor is set very close to the top Ge NWs. In order to eliminate the possible calculation errors, we calculate the absorption by using $A = A_{\text{Ge}} + A_{\text{Au}}$ in this paper. This way the structural effects (including the NW width, height, filling ratio, etc.) on the partial absorptions, A_{Ge} and A_{Au} , and consequently the total absorption, A , can also be studied (see the next section).

3. SIMULATION RESULTS AND DISCUSSION

Figures 2(a), (b) and (c) show the spectra of total absorption, A , and the partial absorption, A_{Ge} and A_{Au} , respectively for the single NW grating absorbers with NW widths of 140 nm (green curve) and 280 nm (red curve), and our SWG-based absorber with $w_1 = w_2 = 140$ nm and $d = 95$ nm (blue curve). We refer these three structures as Case 1, Case 2, and Case 3, respectively for easy description. From Figure 2, it is shown that for all the three cases the absorption in Ge dominates the total absorption in the wavelength range below 1400 nm and there are sharp drops around 1400 nm, beyond which the absorption of Ge indicated by the imaginary part of its refractive index is at least one order of magnitude smaller [35]. Here absorption in Au becomes larger

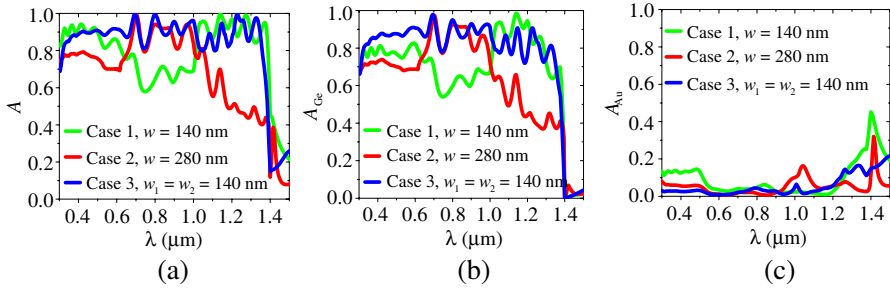


Figure 2. Spectra of (a) total absorption, A ; (b) partial absorption in Ge, A_{Ge} ; and (c) partial absorption in Au, A_{Au} for three cases: Cases 1 and 2 are the single NW grating cases with $w = 140$ nm (green curve) and $w = 280$ nm (red curve); Case 3 is our proposed SWG-based nanostructure with $w_1 = w_2 = 140$ nm and $d = 95$ nm (blue curve). Other structural parameters are: $P = 620$ nm and $h = 1500$ nm.

due to excitations of SPPs, but does not contribute much to the total absorption. In both the Ge absorption and the total absorption spectra shown in Figures 2(a) and (b), ripples can be observed, which are mainly due to the FP interferences between the waves reflected by the bottom Au surface and the grating top surfaces of height, h . Since the grating heights are all the same in the three cases, the small peaks in these absorption spectra appear at almost the same wavelengths. Small deviations can be seen in the long wavelength range between the absorption spectra of Cases 1, 2 and 3 as shown in Figures 2(a) and (b), mainly due to the different filling ratio induced effective refractive indices of the grating films. However, for Cases 2 and 3, which have the same filling ratios, deviations still appear, which will be explained in detail below.

For Cases 1 and 2, three sections appear clearly in the absorption spectra in the wavelength range below 1400 nm as shown in Figures 2(a) and (b). Absorption of Case 1 is higher than that of Case 2 in the ranges of $\lambda < 620$ nm and $\lambda > 1000$ nm, but is lower in the range of $620 \text{ nm} < \lambda < 1000$ nm. According to the diffraction theory, light impinging on a grating will obtain a horizontal wave vector ($m \cdot 2\pi/P$) and the total horizontal wave vector will become $k_x = k_0 \cdot \sin \theta + m \cdot 2\pi/P$, where m is an integer. Under normal incidence, k_x is reduced to $k_x = m \cdot 2\pi/P$. For $\lambda < P = 620$ nm, reflective diffraction are stronger in Case 2 of $w = 280$ nm due to its larger filling ratio and consequently a larger effective refractive index, producing lower absorption than Case 1 of $w = 140$ nm [29]. At $\lambda = 620$ nm, Rayleigh anomaly occurs, where the 1st reflective diffraction order becomes to propagate horizontally along the air-grating surface. Therefore,

absorption increases in Case 2 but decreases in Case 1 where the light experiences less absorbing material as shown in Figures 2(a) and (b). According to the phase-matching condition for the refractive diffractions, that is, $k_x = [k_0 \cdot (1 - w/P) + k_0 n_{\text{Ge}} \cdot w/P] \cdot \sin \theta'_m$, where θ'_m is the refractive diffraction angle of m th diffraction order. For Case 1, the 1st refractive diffraction order becomes another Rayleigh anomaly at $\lambda = 1096$ nm and will propagate horizontally along x direction with $\theta'_m = 90^\circ$. For Case 2, Rayleigh anomaly of the 2nd refractive diffraction order occurs at $\lambda = 822$ nm. For the wavelengths beyond each Rayleigh anomaly, the energy will be redistributed between the remaining diffraction orders, namely, 0-order for Case 1 and 0- and 1-orders for Case 2, of which the 0-order diffraction obtains more energy. Then the FP resonances in the z direction dominate the absorption spectra. In the wavelength range beyond 1000 nm, we find that SPPs are excited at the bottom interface between Ge NW and Au with one and three magnetic field maxima respectively for Cases 1 and 2 as shown in Figures 3(a) and (b). Since the magnetic fields of SPPs are concentrated in the similar way in this wavelength range, only one

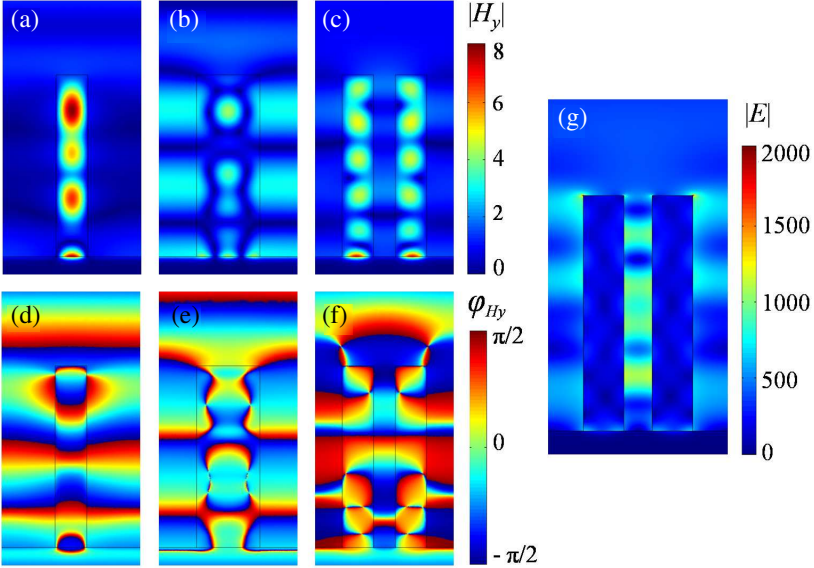


Figure 3. Magnetic field distributions at $\lambda = 1230$ nm: amplitude ($|H_y|$, top row) and phase (φ_{H_y} , bottom row) for three cases: (a), (d) Case 1, (b), (e) Case 2 and (c), (f) Case 3. The structural parameters for each case are the same as those in Figure 2. (g) Electric field distribution, $|E|$, at $\lambda = 1230$ nm for Case 3.

example at $\lambda = 1230$ nm is shown in Figure 3 for all three cases for comparison. For Case 1, the 140 nm-wide Ge NWs (as waveguides) are narrow enough to confine light of long wavelengths as considered here even though most magnetic field is well confined in them as shown in Figure 3(a). Usually wider Ge NWs, e.g., Case 2 with twice width of NW in Case 1, are thought to have much stronger confinement of light than narrower ones. However, the magnetic field in Figure 3(b) shows that much more light is leaking out of the wider (280 nm-wide) NW compared with that of Case 1 in Figure 3(a). From the phase distribution of Case 2 shown in Figure 3(e), it is clearly seen that the phase changes twice along the x direction within the Ge NW, which evolves gradually from the bottom phase induced by the excited higher-order SPP mode at the surface of the Au substrate. Such a phase change along the x direction makes the wider NW worse in light confinement than the narrower half-width NW. In contrary, without any significant phase changes, the phase distribution of Case 1 shown in Figure 3(d) is favorable for a better confinement for photons of long wavelengths shown in Figure 3(a), resulting in better absorptions than Case 2 in this wavelength range as shown in Figures 2(a) and (b).

Interestingly, by introducing a slot into the 280 nm-wide NW in each period, an ultra-broadband absorption spectrum can be achieved for our proposed absorber of Case 3 with the merits of both Cases 1 and 2 as shown in Figures 2(a) and (b). In the short wavelength range below 1000 nm, stronger scattering is generated by the two NWs in each period in Case 3, where the 1st refractive diffraction order experiences more changes of index in comparison with Case 2 of one 280 nm-wide NW in each period, and experiences more absorbing materials in comparison with Case 1 of one 140 nm-wide NWs in each period. Therefore, the absorption spectrum becomes flatter with absorption comparable to that of Case 1 at $\lambda < 620$ nm and to that of Case 2 at $620 \text{ nm} < \lambda < 1000$ nm. In the long wavelength range beyond 1000 nm, SPPs are also generated with well-confined magnetic field at the bottom of each Ge NW. One example at $\lambda = 1230$ nm is shown in Figure 3(c). In comparison with Case 2, the slot inserted in the 280 nm-wide NW totally redistributes the initial phase distribution (shown in Figure 3(e)) of SPPs at the bottom surface of Ge NW, by artificially introducing a minus phase in the slot in contrast with the plus phases in the NWs as shown in Figure 3(f). This results in smooth phase changes along the x direction within each Ge NW and thus a better confinement of the magnetic field. Meanwhile, since the two NWs are separated by a rather small distance of $d = 95$ nm, the evanescent (along the horizontal direction) electric fields of the NWs overlap in the slot, making a much stronger electric field confined in it as shown in Figure 3(g),

for example. This is a typical behavior of light for a high-index slot waveguide [36]. That is why we called the top Ge nanostructure in Case 3 the slot waveguide grating. Quite different from Case 2 with a 280 nm-wide NW in each period, light impinging on the SWG of Case 3 sees a waveguide array of lower effective refractive indices consisting of two NWs and a slot in between in each period. Therefore, more FP fringes are generated in such slot waveguides as shown in Figures 3(c) and (g), leading to the absorption peaks deviated from those of Case 2 as shown in Figures 2(a) and (b). The combined optical effects contribute to the enhanced absorption in this wavelength range compared with Case 2. In general, our proposed SWG-based absorber, Case 3, has a much better absorption performance over the whole wavelength range from 300 to 1400 nm as shown in Figure 2(a). In comparison with the partial absorption spectra shown in Figures 2(b) and (c), Ge SWG itself is a very good absorber and our proposed SWG-based absorber, Case 3, can be exploited further for a high-efficiency photovoltaic solar cell with the Ge SWG as the solar absorber and the Au substrate as the bottom electrode, where the directions of light absorption and free carrier collection can be orthogonalized to further enhance its power conversion efficiency.

From the above spectral analysis, one can learn a little about the effect of NW width on the absorption spectrum. In the following, detailed structural effects are investigated by analyzing average absorptivity, A_{ave} , integrated of the absorption spectrum (not shown here) from 300 to 1400 nm for each structure. Here we follow the above definitions for the three cases for easy comparison and discussion, that is, NW width in Case 2 is twice of that in Case 1 in each period and equal to the total NW width, $w_1 + w_2$, in each period in Case 3 with $w_1 = w_2$. Figure 4(a) shows the relationships of average absorptivity, A_{ave} , vs. NW width, w for Cases 1 and 2, and of A_{ave} vs. $w_1 (= w_2)$ for Case 3, respectively. Other parameters are kept the same, namely, $P = 620$ nm, $h = 1500$ nm and $d = 95$ nm (typically for Case 3). From this figure, one sees that better absorption can be achieved by our proposed absorber in Case 3 than those in both Cases 1 and 2. For Case 3, A_{ave} increases first and then decreases as w increases. A_{ave} reaches its maximum at $w = 140$ nm. With narrower Ge NWs of $w < 140$ nm, photons of short wavelengths rather than those of long wavelengths can be highly absorbed with lower reflection from the SWG. When w increases, the absorption bandwidth increases and A_{ave} increases too. However, when w is larger than 140 nm, reflection becomes even stronger and the whole absorption spectrum becomes lower. Therefore, A_{ave} decreases though long-wavelength photons can be absorbed with more absorbing materials. Similar phenomenon is

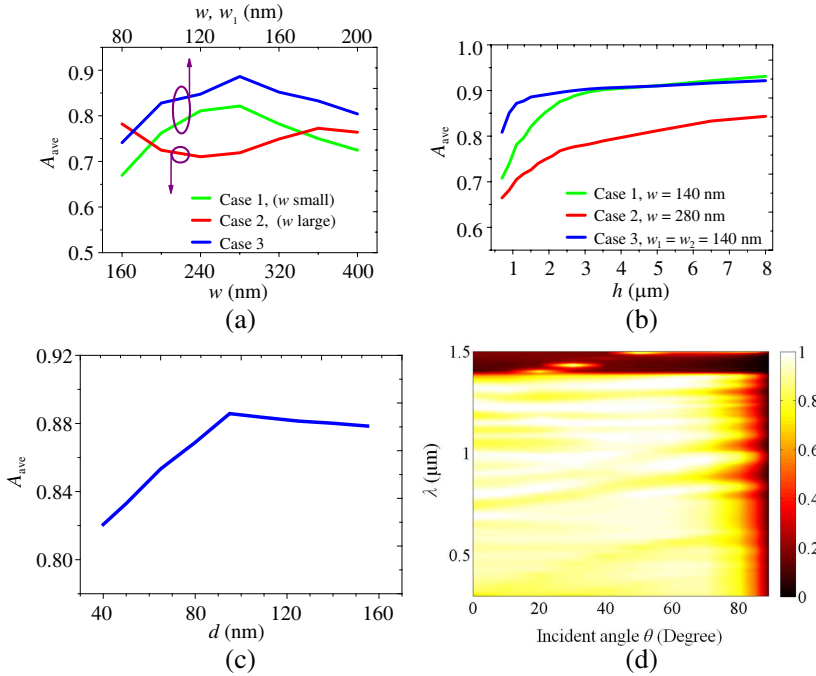


Figure 4. (a)–(c) Average absorptivity, A_{ave} , as functions of different geometric parameters, namely, (a) NW width, w , for Cases 1 and 2, and $w_1 (= w_2)$ for Case 3 with $h = 1.5 \mu\text{m}$ in all three cases; (b) NW height, h , for Cases 1 and 2 with $w = 140$ and 280 nm, and for Case 3 with $w_1 = w_2 = 140$ nm, $d = 95$ nm; (c) slot width, d , for Case 3 with $w_1 = w_2 = 140$ nm, $h = 1.5 \mu\text{m}$. Cases 1–3 are indicated by green, red, and blue curves, respectively. (d) Angle-resolved absorption spectra for Case 3 with $w_1 = w_2 = 140$ nm, $h = 1500$ nm, and $d = 95$ nm. The grating period is set to $P = 620$ nm in all the plots.

observed in Case 1. Different from Case 3, A_{ave} of Case 2 connecting to that of Case 1 increases again when w is larger than 240 nm as shown in Figure 4(a). This is due to the fact that Rayleigh anomaly of the 2-order refractive diffraction red shifts when increasing w . As discussed before, more energy can be consumed by the dominant FP resonances inside Ge NWs beyond the Rayleigh anomaly wavelength. However, the reflection is enhanced at the same time, which results in a decay in absorption when $w > 340$ nm.

For a particular grating with fixed widths of Ge NWs, A_{ave} must increase with NW height, h , since more photons can be absorbed by more absorbing materials. This can be seen from Figure 4(b) for all the three cases. For Case 3, when h is small, A_{ave} is small due to

the insufficient absorption of long-wavelength photons. As h increases, absorption in the long wavelength range starts to increase and the absorption spectra are broadened, thus leading to a fast increase of A_{ave} . When h increases further, A_{ave} rises very slowly and the reflection characteristics become dominant for the total absorption. Compared with Case 3, the fast increase region for A_{ave} is longer for Case 1 and the longest for Case 2. This is due to the fact that more (or the most) absorbing material is needed for Case 1 (Case 2) to compensate the lower absorption spectra shown in Figures 2(a) and (b). When h is larger than $5.2\ \mu\text{m}$, it is seen from Figure 4(b) that A_{ave} becomes a little larger in Case 1 due to the lower reflection than Case 3. For thin-film absorbers, Case 3 is preferred with much higher absorption than both Cases 1 and 2.

Our absorber in Case 3 is featured by a very small slot between the two Ge NWs in each period, which is very important and dominates its absorption characteristics. Figure 4(c) shows that a too small slot degrades the average absorption much since it cannot provide significant scattering in the short wavelength range or significant phase changes at the two interfaces between it and the two NWs in the long wavelength range. In this case, absorber in Case 3 behaves like Case 2 with lower absorption at $\lambda < 620\ \text{nm}$ and $\lambda > 1000\ \text{nm}$ indicated by the red curve in Figure 2(a). A larger slot helps to couple light into it and create phases of opposite signs in it and the NWs. Therefore, A_{ave} increases quickly with d and turns to slowly decrease beyond $d = 95\ \text{nm}$. At $d = 160\ \text{nm}$, Case 3 approximately becomes a single-NW grating with period of $310\ \text{nm}$. Since the evanescent fields in the NWs in adjacent periods are still coupled to each other, A_{ave} does not degrade much from the optimal value of Case 3 at $d = 160\ \text{nm}$.

Angle-resolved absorption spectra of Case 3 are investigated with optimal structural parameters: $P = 620\ \text{nm}$, $w_1 = w_2 = 140\ \text{nm}$, $d = 95\ \text{nm}$, $h = 1.5\ \mu\text{m}$, as shown in Figure 4(d), which indicates the omnidirectional feature. High absorption from 300 to $1400\ \text{nm}$ remains very high until the incident angle, θ , is as large as 80° . In the short wavelength range below about $1000\ \text{nm}$, absorption spectrum dominated by diffraction red shifts when increasing the incident angle, θ . But, in the long wavelength range beyond $1000\ \text{nm}$, since there is no energy redistribution between the diffraction orders, the absorption peaks remain almost unvaried with θ , which are mainly induced by the FP resonances in the z direction. In this wavelength range, angle-sensitive SPPs are excited. However, in Figure 4(d) they are indistinct and covered by the high FP-induced absorption in Ge SWG until they red shift into $\lambda > 1400\ \text{nm}$ where the absorption in Ge SWG is rather low.

By moving the slot horizontally and introducing an asymmetric feature into each period of Case 3, the relationship of A_{ave} vs. w_1 is plotted in Figure 5(a), which shows that a small degree of asymmetry can enhance A_{ave} further to $\sim 90\%$ with $w_1 = 165$ nm, $w_2 = 115$ nm, as compared with 88.6% of the symmetric one with $w_1 = w_2 = 140$ nm. However, A_{ave} drops quickly when a higher degree of asymmetry is introduced. The absorption spectra of the optimal asymmetric SWG-based absorber plotted in Figure 5(b) show that more resonances are excited in the long wavelength range beyond 1000 nm, resulting in a flatter and higher absorption spectrum in comparison with the symmetric one. The partial absorptions, A_{Ge} (blue curve) and A_{Au} (red curve), are shown in Figure 5(c), which indicates that over 86% of

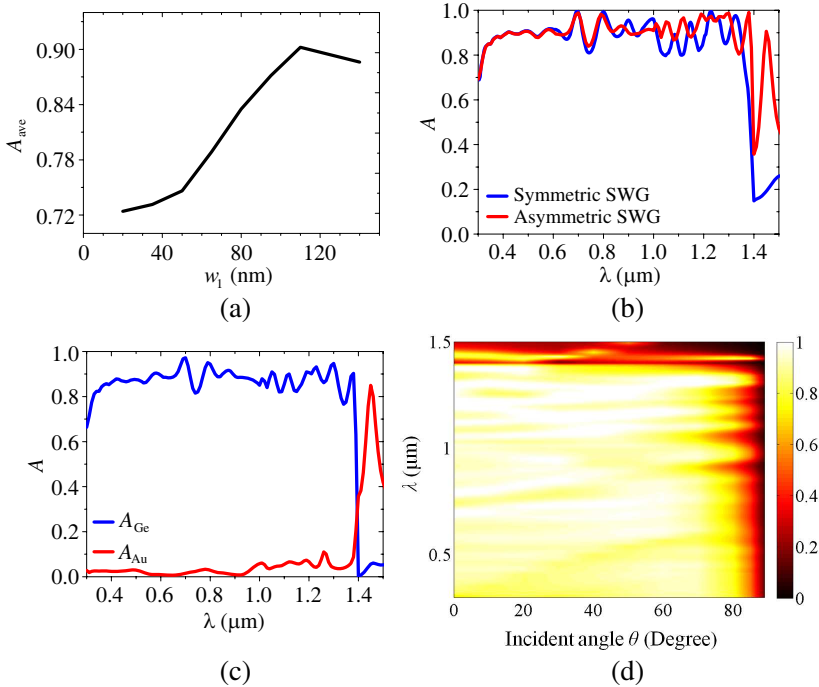


Figure 5. (a) Averaged absorption, A_{ave} , as a function of w_1 with $w_1 + w_2 = 280$ nm. (b) Total absorption spectra, A , for the asymmetric (red curve) and symmetric SWG-based absorber (blue curve). (c) Partial absorption spectra: A_{Ge} (blue curve) and A_{Au} (red curve); (d) Angle-resolved absorption spectra for the asymmetric absorber. For asymmetric absorber in (b)–(d), $w_1 = 165$ nm, $w_2 = 115$ nm; for symmetric absorber in (b), $w_1 = w_2 = 140$ nm. The other geometric parameters in all the four figures are $P = 620$ nm, $h = 1500$ nm, $d = 95$ nm.

the total energy is absorbed by Ge NWs in the range of $300 \text{ nm} < \lambda < 1400 \text{ nm}$. The angle-resolved spectra are investigated in Figure 5(d), and the average absorption reaches over 90% when the incident angle varies between 0 and 80° over a wavelength range from 300 nm to 1400 nm . In the wavelength range beyond 1400 nm , there are two absorption peaks corresponding to SPP-induced high absorption in Au. One is a localized SPP mode, unvaried with θ around $\lambda = 1450 \text{ nm}$. Its magnetic field is concentrated mainly in the 165 nm -wide NW in each period due to the horizontal FP resonance between the SPPs reflected by the NW walls. The other is a propagating SPP mode determined by the phase-matching condition and therefore is quite sensitive to θ . It red shifts quickly beyond 1500 nm at $\theta = 50^\circ$ from 1400 nm under normal incidence. Different from the angle-resolved spectra for the symmetric absorber shown in Figure 4(d), the localized SPPs excited in the asymmetric one further broadens the total absorption spectrum as shown in Figures 5(b) and (d).

4. CONCLUSION

In summary, a perfect absorber consisting of a SWG grating on a gold film has been investigated. For a symmetric SWG, the excellent absorption performance is obtained, of which the average absorption is higher than 88% when the incident angle varies between 0° and 80° over a wavelength range from 300 nm to 1400 nm , meanwhile the average absorption is enhanced by 23% compared with the single NW array with the same total width under the normal incident. An optimized asymmetric NW pair with the same total width can further boost the absorption. This provides us with a new way to realize high efficiency, broadband, and omnidirectional absorption. As our structure is composed of a semiconductor Ge (which dominates the absorption) and gold substrate (which can be used as an electrode), and the present design can be useful for the applications of solar cells and photodetectors, etc. The designed absorber with such a dielectric thin grating is relatively easier to fabricate as compared with other absorbers with metallic nanostructures. Though such high-aspect-ratio grating is not quite easy to fabricate, there are still many methods currently available for fabricating such a high-aspect-ratio structure, e.g., metal-assisted electroless etching [37, 38] and vapor-liquid-solid growth [29, 39]. The present idea can be extended to a three-dimensional case.

ACKNOWLEDGMENT

The authors thank F. Ding, P. P. Xu, and Q. S. Huang for their helpful discussions. This work was partially supported by the National High Technology Research and Development Program (863 Program) of China (No. 2012AA030402), the Zhejiang Provincial Key Project (No. 2011C11024) and National Natural Science Foundation (Nos. 61178062, 61271016, 60901039).

REFERENCES

1. Miles, R. W., K. M. Hynes, and I. Forbes, "Photovoltaic solar cells: An overview of state-of-the-art cell development and environmental issues," *Prog. Cryst. Growth Charact. Mater.*, Vol. 51, 1–42, 2005.
2. Atwater, H. A. and A. Polman, "Plasmonics for improved photovoltaic devices," *Nat. Mater.*, Vol. 9, No. 3, 205–213, 2010.
3. Kraemer, D., et al., "High-performance flat-panel solar thermo-electric generators with high thermal concentration," *Nat. Mater.*, Vol. 10, 532–538, 2011.
4. Watts, C. M., X. Liu, and W. J. Padilla, "Metamaterial electromagnetic wave absorbers," *Adv. Mater.*, Vol. 24, OP98–OP120, 2012.
5. He, S., Y. Cui, et al., "Optical nano-antennas and metamaterials," *Mater. Today*, Vol. 12, No. 12, 16–24, 2009.
6. Schuller, J. A., E. S. Barnard, et al., "Plasmonics for extreme light concentration and manipulation," *Nat. Mater.*, Vol. 9, No. 3, 193–204, 2010.
7. Landy, N. I., et al., "Perfect metamaterial absorber," *Phys. Rev. Lett.*, Vol. 100, No. 20, 207402, 2008.
8. Huang, L. and H. Chen, "Multi-band and polarization insensitive metamaterial absorber," *Progress In Electromagnetics Research*, Vol. 113, 103–110, 2011.
9. Nornikman, H., B. H. Ahmad, M. Z. A. Abdul Aziz, M. F. B. A. Malek, H. Imran, and A. R. Othman, "Study and simulation of an edge couple split ring resonator (EC-SRR) on truncated pyramidal microwave absorber," *Progress In Electromagnetics Research*, Vol. 127, 319–334, 2012.
10. Bonod, N., et al. "Total absorption of light by lamellar metallic gratings," *Opt. Express*, Vol. 16, No. 20, 15431–15438, 2008.
11. Perchec, J. L., P. Quémerais, A. Barbara, and T. López-Ríos, "Why metallic surfaces with grooves a few nanometers deep and

- wide may strongly absorb visible light,” *Phys. Rev. Lett.*, Vol. 100, No. 6, 066408, 2008.
12. Teperik, T. V., et al., “Omnidirectional absorption in nanostructured metal surfaces,” *Nat. Photon.*, Vol. 2, No. 5, 299–301, 2008.
 13. Hao, J., et al., “High performance optical absorber based on a plasmonic metamaterial,” *Appl. Phys. Lett.*, Vol. 96, No. 25, 251104, 2010.
 14. Liu, N., et al., “Infrared perfect absorber and its application as plasmonic sensor,” *Nano Lett.*, Vol. 10, No. 7, 2342–2348, 2010.
 15. He, X.-J., Y. Wang, J. Wang, T. Gui, and Q. Wu, “Dual-band terahertz metamaterial absorber with polarization insensitivity and wide incident angle,” *Progress In Electromagnetics Research*, Vol. 115, 381–397, 2011.
 16. Zhou, H., F. Ding, Y. Jin, and S. He, “Terahertz metamaterial modulators based on absorption,” *Progress In Electromagnetics Research*, Vol. 119, 449–460, 2011.
 17. Ye, Y. Q., Y. Jin, and S. He, “Omnidirectional, polarization-insensitive and broadband thin absorber in the terahertz regime,” *J. Opt. Soc. Am. B*, Vol. 27, No. 3, 498, 2010.
 18. Cui, Y., J. Xu, et al., “A thin film broadband absorber based on multi-sized nanoantennas,” *Appl. Phys. Lett.*, Vol. 99, No. 25, 253101, 2011.
 19. Nielsen, M. G., A. Pors, O. Albrektsen, and S. I. Bozhevolnyi, “Efficient absorption of visible radiation by gap plasmon resonators,” *Opt. Express*, Vol. 20, No. 12, 13311, 2012.
 20. Kravets, V. G., S. Neubeck, et al., “Plasmonic blackbody: Strong absorption of light by metal nanoparticles embedded in a dielectric matrix,” *Phys. Rev. B*, Vol. 81, No. 16, 165401, 2010.
 21. Hedayati, M., et al., “Design of a perfect black absorber at visible frequencies using plasmonic metamaterials,” *Adv. Mat.*, Vol. 23, 5410–5414, 2011.
 22. Aydin, K., et al., “Broadband polarization-independent resonant light absorption using ultrathin plasmonic super absorbers,” *Nat. Commun.*, Vol. 2, 517, 2011.
 23. Søndergaard, T., et al., “Plasmonic black gold by adiabatic nanofocusing and absorption of light in ultra-sharp convex grooves,” *Nat. Commun.*, Vol. 3, No. 969, 22828629, 2012.
 24. Cui, Y., et al., “Ultra-broadband light absorption by a sawtooth anisotropic metamaterial slab,” *Nano Lett.*, Vol. 12, No. 3, 1443–1447, 2011.
 25. Ding, F., et al., “Ultra-broadband microwave metamaterial

- absorber,” *Appl. Phys. Lett.*, Vol. 100, No. 10, 103506–103504, 2012.
26. Kelzenberg, M. D., et al., “Enhanced absorption and carrier collection in Si wire arrays for photovoltaic applications,” *Nat. Mater.*, Vol. 9, 239–244, 2010.
 27. Garnett, E. and P. Yang, “Light trapping in silicon nanowire solar cells,” *Nano Lett.*, Vol. 10, No. 3, 1082–1087, 2010.
 28. Peng, K.-Q., X. Wang, et al., “High-performance silicon nanohole solar cells,” *J. Am. Chem. Soc.*, Vol. 132, No. 20, 6872–6873, 2010.
 29. Fan, Z., et al., “Ordered arrays of dual-diameter nanopillars for maximized optical absorption,” *Nano Lett.*, Vol. 10, No. 10, 3823–3827, 2010.
 30. Huang, Y. F., et al., “Improved broadband and quasi-omnidirectional anti-reflection properties with biomimetic silicon nanostructures,” *Nat. Nano.*, Vol. 2, No. 12, 770–774, 2007.
 31. Zhu, J., et al., “Optical absorption enhancement in amorphous silicon nanowire and nanocone arrays,” *Nano Lett.*, Vol. 9, No. 1, 279–282, 2009.
 32. Yang, L., L. Mo, Y. Okuno, and S. He, “Optimal design of ultra-broadband, omnidirectional, and polarization-insensitive amorphous silicon solar cells with a core-shell nanograting structure,” *Prog. Photovolt.: Res. Appl.*, 2012, DOI: 10.1002/pip.2206.
 33. Luque, A. and S. Hegedus, *Handbook of Photovoltaic Science and Engineering*, Wiley, 2003.
 34. Jin, J. M., *The Finite Element Method in Electromagnetics*, John Wiley & Sons, 1993.
 35. Palik, E. D., *Handbook of Optical Constants of Solids*, Academic, New York, 1985.
 36. Almeida, V. R., et al., “Guiding and confining light in void nanostructure,” *Opt. Lett.*, Vol. 29, No. 11, 1209–1211, 2004.
 37. Peng, K., Y. Wu, et al., “Uniform, axial-orientation alignment of one-dimensional single-crystal silicon nanostructure arrays,” *Angew. Chem.-Int. Edit.*, Vol. 44, No. 18, 2737–2742, 2005.
 38. Weisse, J. M., D. R. Kim, et al., “Vertical transfer of uniform silicon nanowire arrays via crack formation,” *Nano Lett.*, Vol. 11, No. 3, 1300–1305, 2011.
 39. Wagner, R. S. and W. C. Ellis, “Vapor-liquid-solid mechanism of single crystal growth,” *Appl. Phys. Lett.*, Vol. 4, No. 5, 89–90, 1964.